Structural Properties of Catalytically Active Bimetallic Gold-Palladium Nanoparticles Synthesized on Rutile Titania Nanorods by Pulsed Laser Deposition

N. Tai Nguyen, J. Nelayah, P. Afanasiev, L. Piccolo, D. Alloyeau, C. Ricolleau

To cite this version:

N. Tai Nguyen, J. Nelayah, P. Afanasiev, L. Piccolo, D. Alloyeau, et al.. Structural Properties of Catalytically Active Bimetallic Gold-Palladium Nanoparticles Synthesized on Rutile Titania Nanorods by Pulsed Laser Deposition. Crystal Growth & Design, 2018, 18 (1), pp.68-76. 10.1021/acs.cgd.7b00708. hal-01692478

HAL Id: hal-01692478

https://hal.science/hal-01692478

Submitted on 15 Nov 2023

Structural properties of catalytically-active bimetallic gold-palladium nanoparticles synthesized on rutile titania nanorods by pulsed laser deposition

N. Tai Nguyen,# Jaysen Nelayah,#, Pavel Afanasiev, † Laurent Piccolo, †,* Damien Alloyeau,# Christian Ricolleau#*

 # Université Paris Diderot, Sorbonne Paris Cité, CNRS, Laboratoire Matériaux et Phénomènes Quantiques, UMR 7162, 75013, Paris, France

† Institut de recherches sur la catalyse et l'environnement de Lyon (IRCELYON), UMR 5256 CNRS & Université Claude Bernard – Lyon 1, 2 avenue Albert Einstein, 69626 Villeurbanne, France.

Gold-palladium nanoparticles with the average size of 3.5 nm and controlled compositions were grown on rutile titania nanorods using pulsed laser deposition. The structural properties of the as-synthesized nanoparticles and their interface with the oxide support were studied at the atomic scale using aberration-corrected transmission electron microscopy. High resolution TEM imaging showed that both polycrystalline Au-Pd particles with droplet morphology and single-crystalline particles with truncated octahedron morphology were stabilized on the nanorods during laser deposition depending on the degree of epitaxy between the nanoparticles and the oxide support. By analyzing the single-crystalline particles formed in the presence of a strong epitaxy, eleven epitaxial relationships between the Au-Pd nanoparticles and their supports were identified with the two dominant ones being: Au-Pd (111) [101] // r-TiO_2(110) [1-1-1] and Au-Pd (100) [101] // r-TiO2 (110) [1-10]. Catalytic testing of the bimetallic titania-supported Au-Pd nanoparticles in the partial hydrogenation of 1,3-butadiene showed that they were both active and selective for this reaction. An increase in the catalytic stability with the gold content was evidenced.

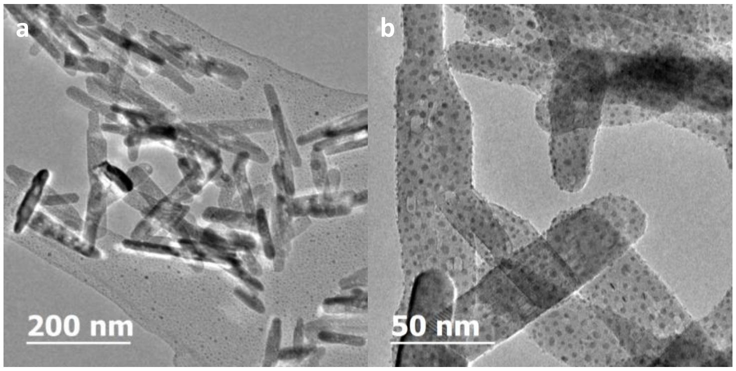

**Corresponding authors : E-mail : jaysen.nelayah@univ-paris-diderot.fr,*

laurent.piccolo@ircelyon.univ-lyon1.fr

Structural properties of catalytically-active bimetallic gold-palladium nanoparticles synthesized on rutile titania nanorods by pulsed laser deposition

N. Tai Nguyen,# Jaysen Nelayah,#, Pavel Afanasiev, † Laurent Piccolo, †,* Damien Alloyeau,# Christian Ricolleau#*

 # Université Paris Diderot, Sorbonne Paris Cité, CNRS, Laboratoire Matériaux et Phénomènes Quantiques, UMR 7162, 75013, Paris, France

† Institut de recherches sur la catalyse et l'environnement de Lyon (IRCELYON), UMR 5256 CNRS & Université Claude Bernard – Lyon 1, 2 avenue Albert Einstein, 69626 Villeurbanne, France.

- **Abstract**

Gold-palladium nanoparticles with the average size of 3.5 nm and controlled compositions were grown on rutile titania nanorods using pulsed laser deposition. The structural properties of the as-synthesized nanoparticles and their interface with the oxide support were studied at the atomic scale using aberration-corrected transmission electron microscopy. High resolution TEM imaging showed that both polycrystalline Au-Pd particles with droplet morphology and single-crystalline particles with truncated octahedron morphology were stabilized on the nanorods during laser deposition depending on the degree of epitaxy between the nanoparticles and the oxide support.

By analyzing the single-crystalline particles formed in the presence of a strong epitaxy, eleven epitaxial relationships between the Au-Pd nanoparticles and their supports were identified with the two dominant ones being: Au-Pd (111) [101] // r-TiO_2(110) [1-1-1] and Au-Pd (100) [101] // r-TiO2 (110) [1-10]. Catalytic testing of the bimetallic titania-supported Au-Pd nanoparticles in the partial hydrogenation of 1,3-butadiene showed that they were both active and selective for this reaction. An increase in the catalytic stability with the gold content was evidenced.

▪ INTRODUCTION

The combination of several metals has been long known as an important way of improving the activity, selectivity and/or stability of heterogeneous catalysts. In recent years, the renewed interest for nanoalloys, i.e. well-defined multimetallic nanoparticles, has been driven by great advances in atomic-scale characterization (e.g., aberration-corrected TEM) and structural simulation techniques. In heterogeneous catalysis, this has allowed researchers to better model and understand surface reaction processes, thereby enabling a rational design of more efficient catalysts[1]. Au-Pd is probably the most investigated catalytic bimetallic system, due to the efficiency of Au-Pd catalysts in various reactions such as synthesis of vinyl acetate monomer[2], synthesis of hydrogen peroxide[3], oxidation of primary alcohols to aldehydes[4], and selective hydrogenations[5,6,7,8], among many others.

The partial hydrogenations of alkynes or alkadienes to form alkenes are applied in the chemical industry for polymer production and use palladium-based catalysts. Palladium is very selective at high concentrations of alkyne or alkadiene impurities. Nevertheless, in case of low concentrations, palladium is not selective enough to completely remove all traces of impurities. Besides, secondary polymerization of alkenes cannot be avoided and palladium is also susceptible to poisoning by various oligomers (or “green oil”) during hydrogenation[9]. In contrast to palladium, gold is inert in the bulk state[10]. However, supported gold nanoparticles recently showed interesting performance for the selective hydrogenation[11,12]. Supported gold particles with sizes between 2 and 5 nm, even if they are less active than palladium, are much more selective in the partial hydrogenation of alkynes or alkadienes[4]. Compared with palladium and other group VIII metals, the low catalytic activity of gold is mostly due to the small number of active sites able to dissociate adsorbed hydrogen molecules[13].

With the increasing use of supported Au-Pd NPs as heterogeneous catalysts, their preparation has been intensively studied in recent years. Different strategies based on both chemical and physical methods have been implemented to synthesize supported Au-Pd bimetallic catalysts, along with their monometallic counterparts. For chemical routes, two main strategies have been introduced to prepare supported Au-Pd NPs: impregnation-like and sol-immobilization techniques[14,15,16,17]. With respect to impregnation methods, colloidal chemical reduction followed by sol immobilization enables a better tuning of particle morphology and composition, however particle size remains poorly controlled during alloy formation. Thus, developing new chemical routes to bimetallic catalysts with fine control of particle size, morphology and composition is still a key challenge in the field of catalysis. A physical route using pulsed laser deposition (PLD) in alternate mode has recently been implemented to produce monometallic Au and Pd NPs as well as bimetallic Au-Pd NPs. With this method, NPs with tuned particle size and composition can be deposited on any support. For instance, in previous works, we have succeeded in immobilizing Au-Pd NPs of various compositions on both amorphous carbon and crystalline supports (NaCl, MgO, ZrO_2 and TiO_2)[18,19].

Here, on the basis of aberration-corrected electron microscopy analyses, we first report on the structure and the equilibrium shape of nanometer-sized monometallic Au and Pd NPs and bimetallic Au-Pd NPs fabricated by pulsed laser deposition onto TiO_2-rutile nanorods exposing (110) facets. In particular, the epitaxial relationships of the Au-Pd NPs with the oxide support are studied as a function of the particle composition. We then illustrate the potential of the as-grown supported Au-Pd NPs as model catalysts for the selective hydrogenation of 1,3-butadiene. In particular, the effect of alloying gold with palladium on the catalytic activity, selectivity and stability is investigated by comparing the catalytic performances of the monometallic Pd and bimetallic Au-Pd NPs.

▪ EXPERIMENTAL SECTION

Gold-palladium NPs were synthesized by the pulsed laser deposition (PLD) technique in a high vacuum chamber (~10^{-7} Torr). Au-Pd particles were deposited on hydrothermally obtained rutile titania (r-TiO_2) nanorods [20,21]. Before metal deposition, the nanorods were first washed two times with ammonium nitrate to remove adsorbed sulfate and then calcined in air. It results in an impurity level at the surface of the nanorods of less than 0.1 %. The r-TiO_2 nanorods were dispersed on different substrates depending on the characterization method. For transmission electron microscopy (TEM), we used standard copper TEM grids (holey carbon on a 400 mesh Cu grid from Agar Scientifics). For catalytic tests, square mica sheets of 11 mm x 11 mm x 0.15 mm size were used to provide the quantity of metallic phase sufficient for detecting its catalytic activity. The substrate holder in the vacuum chamber is designed to enable simultaneous deposition of metals on various supports having different sizes. Regardless of the substrate nature, during laser deposition the nanorods were heated at 300°C using a proportional-integral-derivative controller (Eurotherm). The deposition process was done by using a KrF laser at 248 nm with a repetition rate of 5 Hz and pulse duration of 25 ns (COMPexPro 102F, COHERENT®). Depending on ablation threshold of gold and palladium, the pulse energy at the exit of the laser was adjusted between 250 and 400 mJ. Bimetallic Au-Pd nanoalloys were fabricated by alternately ablating two ultrapure monometallic gold and palladium targets (99.99% purity). The deposition process was divided in sequences to form homogeneous alloy compositions. For each sequence, the total thickness of the deposited metals was fixed to 1 Å. Prior to deposition, the deposition rate of each metal was controlled by an *in situ* quartz balance (INFICON). This set-up enables a precise control of both the composition and the metal quantity in the deposited alloy. The nominal thickness deposited (which corresponds to the total thickness of metals deposited in a continuous thin film approximation) was fixed at 1 nm to synthesize well-separated NPs of a few nm size. The two target compositions for this study were $Au_{57}Pd_{43}$ and $Au_{38}Pd_{62}$. Pure Au and pure Pd NPs were also prepared.

The structural properties of the model catalysts were studied by high-resolution TEM (HRTEM) imaging using a Jeol ARM 200F electron microscope. This microscope combines a last-generation cold-field emission gun[22] and a CEOS hexapole corrector[23] (CEOS GmbH) to compensate for the spherical aberration of the objective lens. This microscope can achieve a point resolution of 75 pm at 200 kV or 115 pm at 80 kV[24]. To avoid structural modifications of supported nanoparticles due to the high-energy electron beam, high-resolution images were acquired at 80 kV.

Sample compositions were determined using TEM energy dispersive X-ray spectroscopy (TEM-EDS) by analyzing the intensities of the Au-$M_{\alpha,\beta}$ (between 2.00 and 2.24 keV) and Pd-$L_{\alpha,\beta}$ (between 2.70 and 2.94 keV) peaks using the Cliff-Lorimer method[25]. The Cliff-Lorimer K-factor used for quantification was experimentally determined by using a thin wedge-shaped $Au_{48}Pd_{52}$ film fabricated by PLD and thinned by focused ion beam milling (PIPS™, GATAN). Prior to thinning, the composition of the film was precisely determined by inductively coupled plasma optical emission spectrometry. Note that the NP composition corresponds to the mean value determined by TEM-EDS measurements made on large NP assemblies. The uncertainty on the atomic composition is estimated to be ± 1 at.%.

Catalytic testing in selective hydrogenation of 1,3-butadiene was carried out in a static stainless-steel reaction cell (volume ~ 120 cm^3) combined with an UHV preparation/characterization setup.[26] Prior to the tests, the reactant gases (research-grade purity) were mixed in a separate UHV chamber. The catalytic tests were performed at room temperature under hydrogen-rich C_4H_6:H_2 conditions with initial pressures of 0.5 Torr C_4H_6 and 5 Torr H_2. 0.5 Torr argon was also present in the gas mixture for internal calibration. The reaction kinetics was continuously tracked by sampling the gases through a leak valve and analyzing them by mass spectrometry. The peak intensities for m/z = 2, 40, 54, 56 and 58 were recorded to determine the partial pressures of H_2, Ar, C_4H_6 (1,3-butadiene), C_4H_8 (butenes, the three isomers could not be distinguished) and C_4H_{10} (butane), respectively. After normalizing by the Ar signal, the data were corrected for ion fragmentation and spectrometer sensitivity to obtain partial pressures.[27] In order to assess the catalyst stability, repeated reaction runs separated by evacuation periods (secondary vacuum) were performed for each sample. Activation/regeneration treatments at 300 °C in O_2 and H_2 (10 Torr, 30 min) were also carried out in the reactor using laser heating.[26]

RESULTS AND DISCUSSION

Au_xPd_{1-x} nanoparticles with different compositions were fabricated on r-TiO_2 nanorods. Figure 1a shows a TEM bright field image of the nanorods dispersed on a holey carbon film. Those nanorods present an oblong shape (100-500nm in length and 20-40 nm in thickness) and are oriented along the [001] direction of the r-TiO_2 structure. Moreover, they selectively expose 95-98% of (110) facets and their specific surface area is 60-65 m²/g[20]. The morphology of the NPs after the deposition of Au and Pd atoms by PLD is shown in Figure 1b.

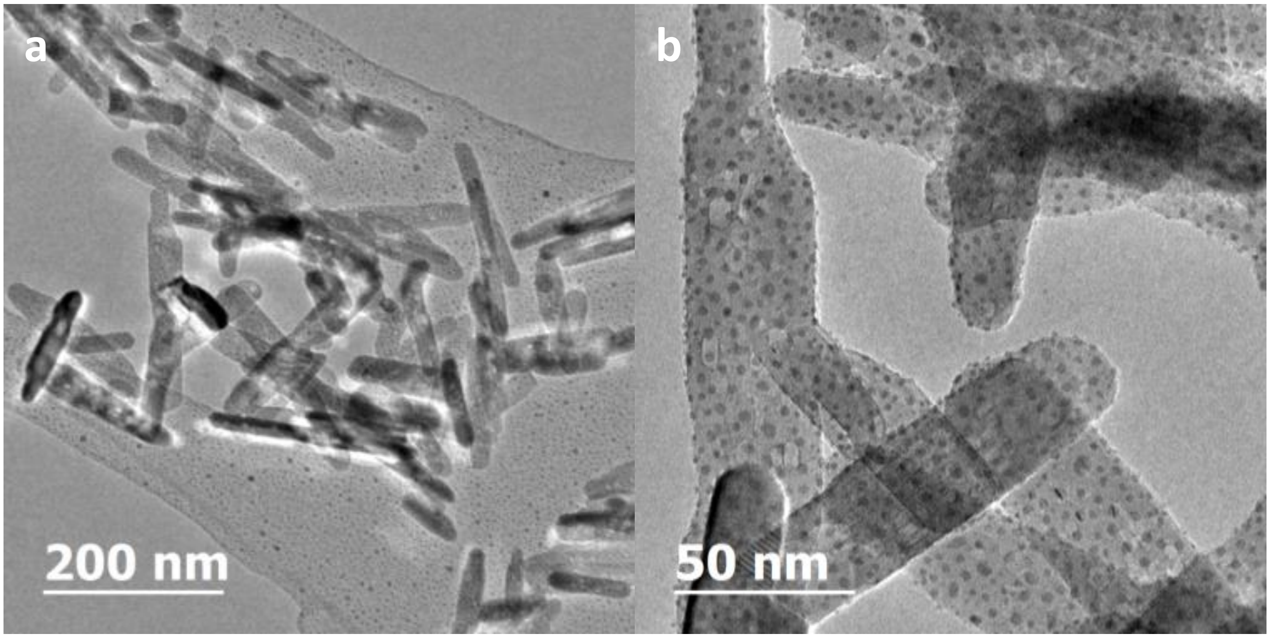

Figure 1 : (a) Low magnification TEM bright field images of rutile titania (r-TiO_2) nanorods dispersed on holey carbon support film. (b) Au-Pd NPs fabricated by PLD deposited on the r-TiO_2 nanorods.

High resolution TEM images of as-grown monometallic Au and Pd NPs as well as Au-Pd bimetallic NPs on r-TiO_2 nanorods are shown in Figure 2 for four different samples: (a) Au/r-TiO_2, (b) $Au_{57}Pd_{43}$/r-TiO_2, (c) $Au_{38}Pd_{62}$/r-TiO_2 and (d) Pd/r-TiO_2. Regardless of sample composition, the supported particles display a variety of shapes. For all four samples, the average projected area diameter of particles (*i.e.* the diameter of a perfect circle enclosing an area equivalent to the projection area of a particle) is mostly below 10 nm and it follows a narrow distribution with a mean diameter of ~3.5 nm when excluding NPs with diameter above 10 nm (see inserts of Figure 2). These large NPs result from the coalescence of smaller ones during particle growth. Since their appearance frequencies are very low, they are not considered for size-distribution analyses. Moreover, the majority of the particles are polycrystalline with droplet morphology or twinned structure. The presence of defects and the droplet morphology are strong indications of a weak degree of epitaxy between Au-Pd particles and r-TiO_2 supports. However, some well-defined single-crystalline particles with truncated octahedron morphology were also observed. The presence of those particles on smooth r-TiO_2 surfaces enabled structure determination and identification of epitaxial relationships between the nanoparticles and the r-TiO_2 nanorods.

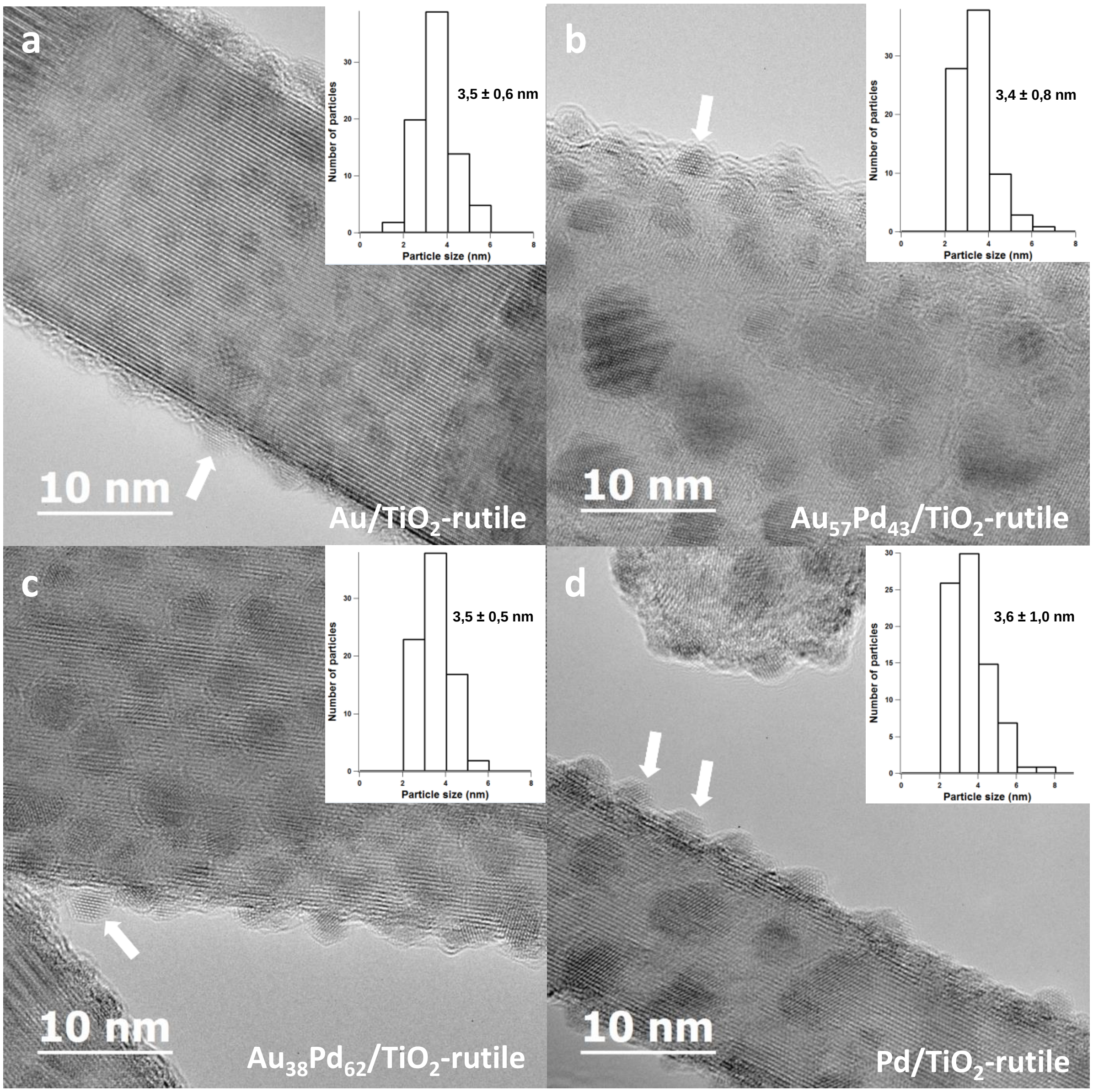

Figure 2 : HRTEM images of different particles supported on r-TiO_2: (a) Au/r-TiO_2; (b) $Au_{57}Pd_{43}$/r-TiO_2; (c) $Au_{38}Pd_{62}$/r-TiO_2; (d) Pd/r-TiO_2. For each sample, the particle size distribution for particles with diameter below 10 nm is shown in insert. The average in-plane particle size is ~3.5 nm for all samples. Particles with truncated octahedron shape are indicated by white arrows.

Figure 3 presents HRTEM images of four nanoparticles for each sample. The corresponding Fourier transforms (FT) and epitaxial relationships are shown in the inserts. According to the FTs, those particles are single crystals and, except Fig. 3k, present a face-centered cubic (FCC) structure oriented along the [101] zone axis and exhibit a truncated octahedron shape bounded by {111} and {100} facets. This morphology is compatible with the equilibrium shape of free Au-Pd particles predicted in the work of Ringe *et al.*[28] In the case of Figure 3k, the particle shows a square/rectangular morphology delimited by {110} and {100} facets and oriented along the [001] zone axis of the FCC structure.

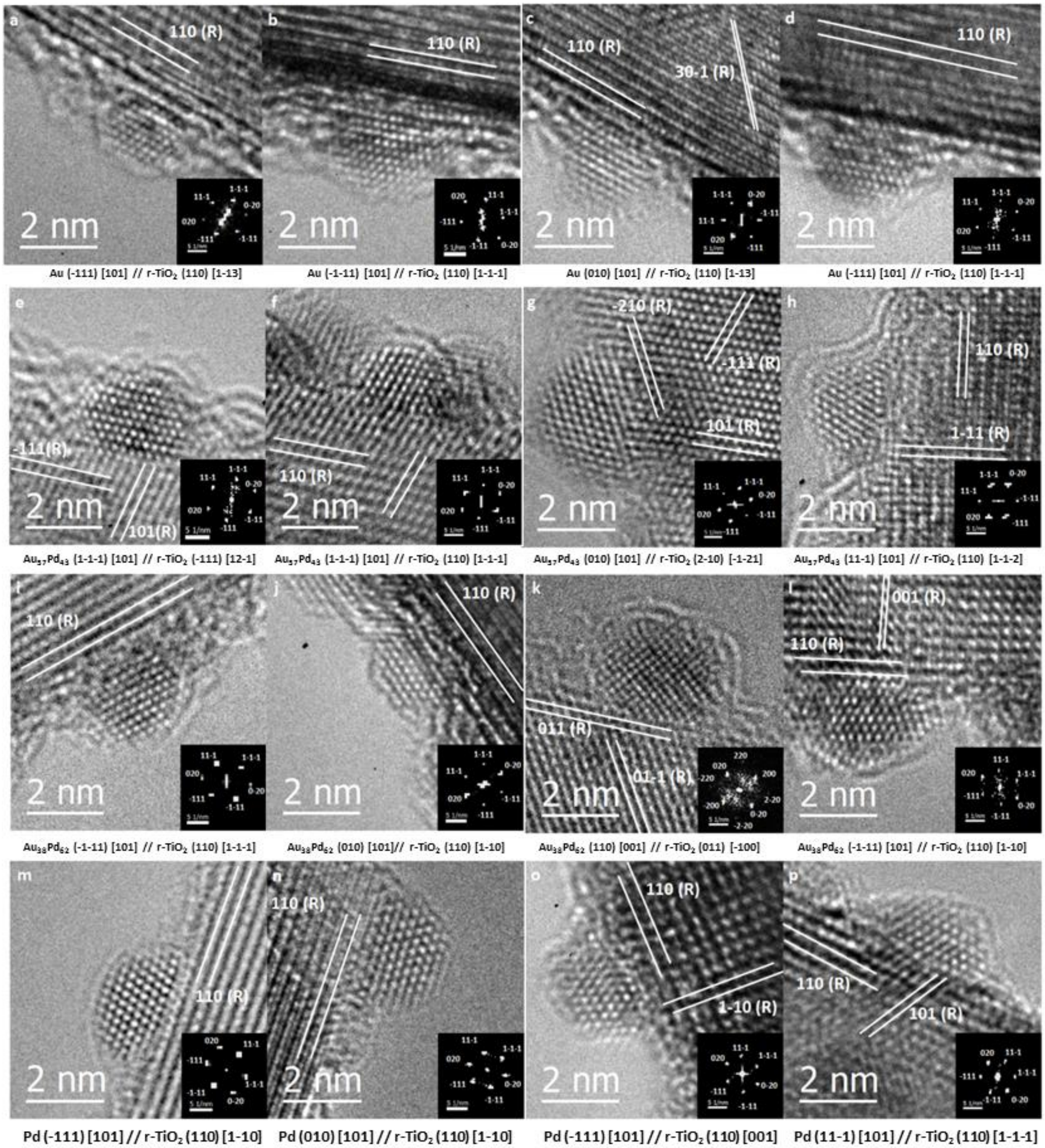

Au (-111) [101] // r-TiO$_2$ (110) [1-13]
Au (-1-11) [101] // r-TiO$_2$ (110) [1-1-1]
Au (010) [101] // r-TiO$_2$ (110) [1-13]
Au (-111) [101] // r-TiO$_2$ (110) [1-1-1]

Au$_{57}$Pd$_{43}$ (1-1-1) [101] // r-TiO$_2$ (-111) [12-1]
Au$_{57}$Pd$_{43}$ (1-1-1) [101] // r-TiO$_2$ (110) [1-1-1]
Au$_{57}$Pd$_{43}$ (010) [101] // r-TiO$_2$ (2-10) [-1-21]
Au$_{57}$Pd$_{43}$ (11-1) [101] // r-TiO$_2$ (110) [1-1-2]

Au$_{38}$Pd$_{62}$ (-1-11) [101] // r-TiO$_2$ (110) [1-1-1]
Au$_{38}$Pd$_{62}$ (010) [101]// r-TiO$_2$ (110) [1-10]
Au$_{38}$Pd$_{62}$ (110) [001] // r-TiO$_2$ (011) [-100]
Au$_{38}$Pd$_{62}$ (-1-11) [101] // r-TiO$_2$ (110) [1-10]

Pd (-111) [101] // r-TiO$_2$ (110) [1-10]
Pd (010) [101] // r-TiO$_2$ (110) [1-10]
Pd (-111) [101] // r-TiO$_2$ (110) [001]
Pd (11-1) [101] // r-TiO$_2$ (110) [1-1-1]

Figure 3 : HRTEM images and corresponding Fourier transforms (inserts) of truncated octahedron Au_xPd_{1-x} nanoparticles supported on TiO_2-rutile: (a-d) pure Au; (e-h) $Au_{57}Pd_{43}$; (i-l) $Au_{38}Pd_{62}$; (m-p) pure Pd. The epitaxial relationships are indicated under each images. The crystallographic planes of the rutile support are also indexed.

Although the particle-rutile interface is not always well-defined, the HRTEM imaging permits the identification of several epitaxial relationships. Note that the epitaxial relationships for a given NP/support are presented as follows: “Particle (hkl) [uvw] // Support (h’k’l’) [u’v’w’]” where (hkl) and (h’k’l’) are the Miller indexes of the planes of the NP and of the support in contact, respectively; [uvw] and [u’v’w’] are two directions, which are parallel to each other and parallel to the NP/support interface. Eleven epitaxial relationships were determined when grouping epitaxies that are equivalent from a crystallographic point of view. The results are summarized in Table 1, where symmetry-equivalent connecting planes of the NPs belonging to the {100}, {110} and {111} families are denoted by common indexes (100), (110) and (111), respectively.

Epitaxial relationship	**Au**	**$Au_{57}Pd_{43}$**	**$Au_{38}Pd_{62}$**	**Pd**	**Total**
(110) [001] // r-TiO_2 (011) [-100]	0	0	3	0	3
(100) [101] // r-TiO_2 (110) [1-10]	0	2	11	5	18
(111) [101] // r-TiO_2 (110) [1-10]	0	1	3	6	10
(111) [101] // r-TiO_2 (110) [1-1-1]	3	12	6	11	32
(111) [101] // r-TiO_2 (110) [1-13]	1	0	0	0	1
(100) [101] // r-TiO_2 (110) [1-13]	1	0	0	0	1
(100) [101] // r-TiO_2 (210) [-120]	0	1	0	0	1
(100) [101] // r-TiO_2 (2-10) [-1-21]	0	1	0	0	1
(111) [101] // r-TiO_2 (-111) [12-1]	0	3	0	0	3
(111) [101] // r-TiO_2 (110) [1-1-2]	0	2	0	0	2

(111) [101] // r-TiO$_2$ (110) [001]	0	0	0	1	1
Total	5	22	23	23	73

Table 1: Epitaxial relationships and corresponding frequencies of occurrence in Au$_x$Pd$_{1-x}$ *nanoparticles fabricated by pulsed laser deposition on* r-TiO$_2$ *nanorods.*

For Au, the small number of observations is due to the limited presence of truncated octahedron particles and to the difficulty of precise determination of epitaxial relationships. This weak degree of epitaxy of Au/r-TiO$_2$ was already reported in several studies on the growth of NPs on r-TiO$_2$ (110) single crystal[29–32]. However, when the epitaxy exists, the configuration is mostly Au (111) // r-TiO$_2$ (110) with weak alignment between Au [101] and r-TiO$_2$ [001] directions[33,34]. Note that none of the three relationships found here have been previously reported in the literature.

Concerning Pd, the dominant epitaxial relationship, Pd (111) [101] // r-TiO$_2$ (110) [1-1-1], has never been experimentally observed to the best of our knowledge. The only documented configuration is Pd (111) [101] // r-TiO$_2$ (110) [1-10]. It is equivalent to the relationship Pd (111) [1-21] // r-TiO$_2$ (110) [001], observed by Suzuki and Souda using RHEED on Pd films epitaxially formed on freshly cleaved TiO$_2$ (110) single crystal[35]. This epitaxy was also observed by scanning tunneling microscopy in truncated octahedral Pd NPs stabilized on TiO$_2$ (110) single crystal[36,37,38].

In order to determine the orientation relationship between two crystals, the calculation of coincidence of reciprocal lattice points (CRLP) is a powerful method. This method is used to determine the lattice matching between two crystals in reciprocal space[39]. In the case of the Au / r-TiO$_2$ system, Akita *et al.* have shown that there is no preferential epitaxy between the two materials since several orientation relationships are possible[40]. In addition, these unexpected results for Au and Pd can be explained by the surface roughness of r-TiO$_2$ nanorods.

In the case of Au-Pd nanoalloys, the two dominant epitaxial relationships, Au-Pd (111) [101] // r-

TiO_2 (110) [1-1-1] and Au-Pd (100) [101] // r-TiO_2 (110) [1-10], are described in detail below. Figure 4a presents a HRTEM image of an $Au_{57}Pd_{43}$ NP on r-TiO_2, which shows the configuration Au-Pd (111) [101] // r-TiO_2 (110) [1-1-1]. The crystallographic planes of the particle and its support are also shown. An alignment between (11-1) planes of the particle and (101) planes of TiO_2-rutile is observed. This alignment can be easily explained from crystallographic considerations. In the FCC structure, the angle between (11-1) and (1-1-1) planes is equal to 70.5°, which is very close to the angle between (101) and (110) planes in the tetragonal structure of r-TiO_2, 67.5°. The FTs of rutile support and Au-Pd particle have been indexed to the corresponding tetragonal and cubic structures of r-TiO_2 and AuPd (Figure 4b and c, respectively). The rutile support is oriented along [1-1-1] zone axis and the particle is oriented along [101] zone axis. A structural model of this Au-Pd NP supported on TiO_2 is shown in Figure 4d in cross section.

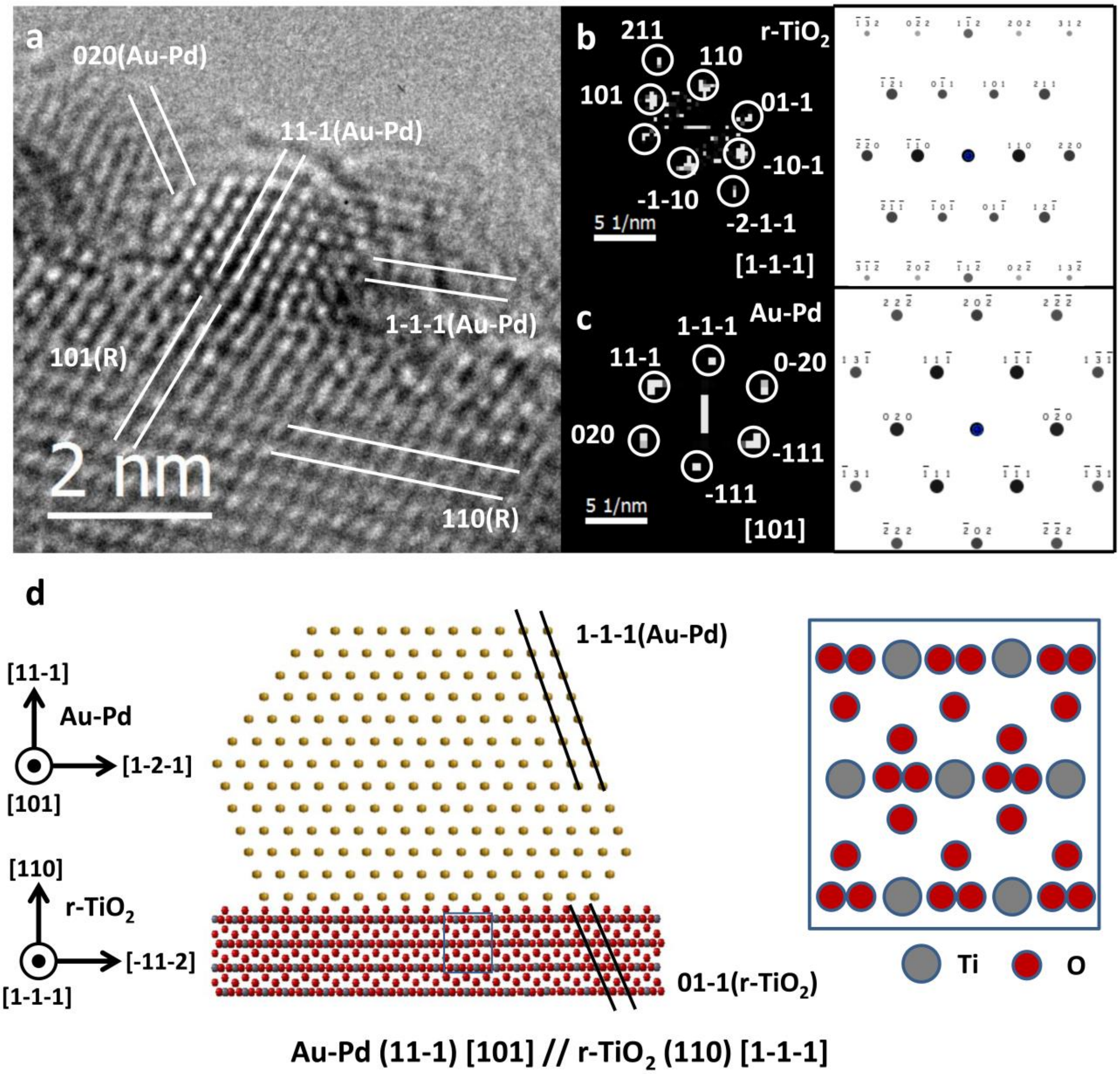

Figure 4 : Example of epitaxial relationship Au-Pd (111) [101] // r-TiO$_2$ (110) [1-1-1]: (a) HRTEM image of an Au-Pd NP supported on r-TiO$_2$; (b) Electron diffraction pattern of the rutile structure along the [1-1-1] zone axis; (c) Electron diffraction pattern of the Au-Pd NP along the [101] zone axis; (d) Model of an Au-Pd NP supported on TiO$_2$ corresponding to Au-Pd (111) [101] // r-TiO$_2$ (110) [1-1-1] epitaxial relationship.

Figure 5a presents a HRTEM image of a supported Au-Pd particle corresponding to the configuration Au-Pd (100) [101] // r-TiO$_2$ (110) [1-10]. The plane alignment is less obvious than for the previous case but can be determined by the FTs analysis, which confirms that rutile is oriented along [1-10] zone axis while the particle is oriented along [101] zone axis. By comparison with the simulated pattern (right-hand side of Fig. 5b), one can note the presence of additional 001 reflection spots, which can be explained by a slight tilt deviation from the exact [1-10] zone axis orientation. A structural model of this Au-Pd NP supported on TiO_2 is shown in Figure 5d in cross section. The alignment between (20-2) planes of the Au-Pd NP and (002) planes of r-TiO_2 is clearly seen in this configuration.

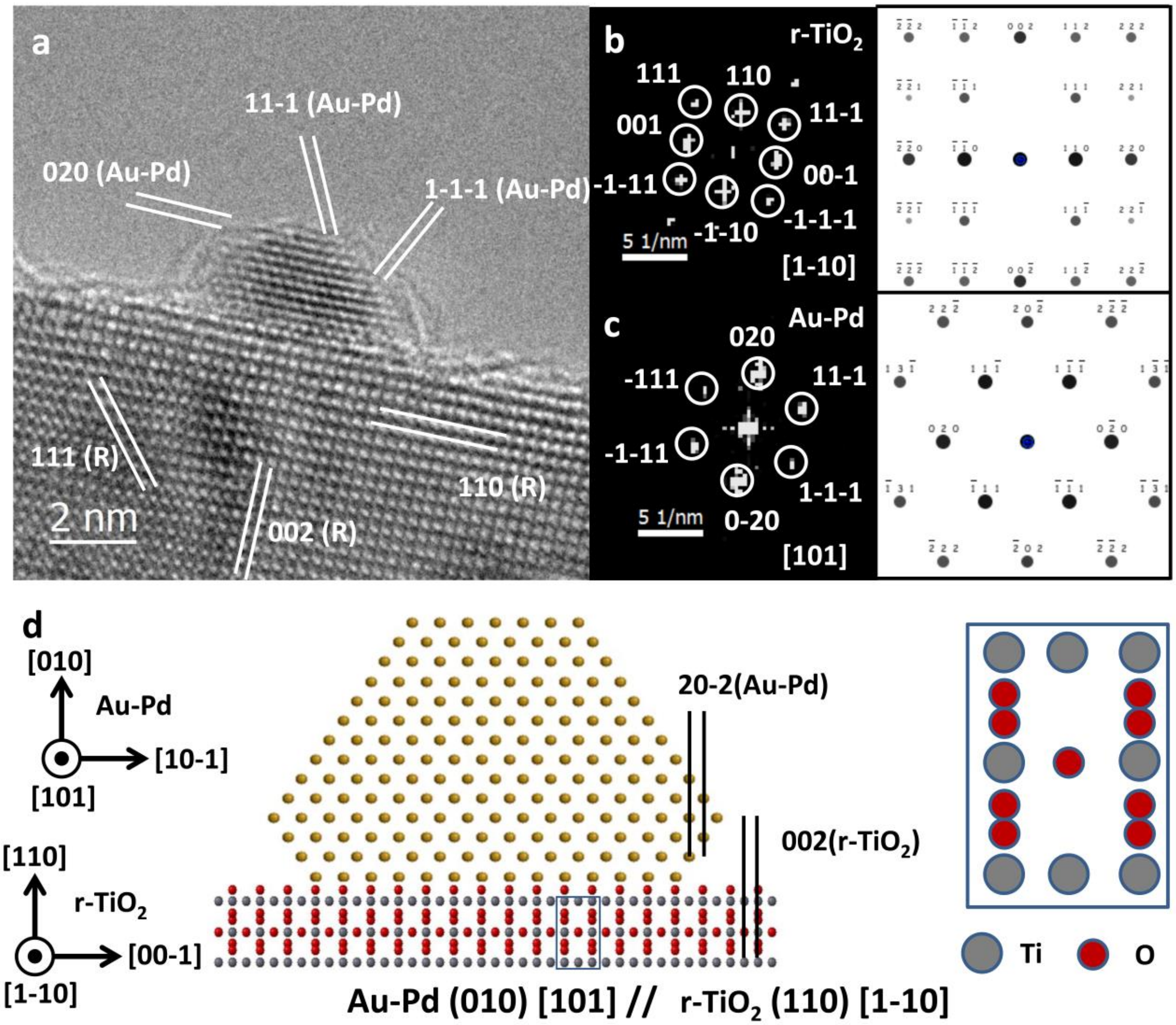

Figure 5 : Example of epitaxial relationship Au-Pd (100) [101] // r-TiO_2 (110) [1-10]: (a) HRTEM

image of an Au-Pd NP supported on r-TiO_2*; (b) Electron diffraction pattern of the rutile structure along the [1-10] zone axis; (c) Electron diffraction pattern of the Au-Pd structure along the [101] zone axis; (d) Model of an Au-Pd NP supported on* TiO_2 *corresponding to Au-Pd (100) [101] // r-*TiO_2 *(110) [1-10] epitaxial relationship.*

In bimetallic solid-solution nanoalloys, it has been reported that the lattice parameter varies linearly with the composition, according to Vegard's law[41]. For both previous cases, we can thus determine the NPs composition by measuring their lattice parameter using the FTs of the HRTEM images. The lattice parameters of the NPs shown in Figures 4a and 5a are equal to 4.00 Å and 3.97 Å, respectively. Given the lattice parameter of pure Au (4.08 Å) and Pd (3.89 Å) bulk phases, the composition of an alloy containing x % at. Pd is given by:

$$x_{Pd} = \frac{\boldsymbol{a_{exp}-4.078}}{\boldsymbol{(3.890-4.078).10^{-2}}}$$

where a_{exp} is the alloy lattice parameter deduced from the HRTEM images. This gives x_{Pd} = 43.6% at. for the NP in Fig. 4a and x_{Pd} = 55.9 % at. for the NP in Fig. 5a. Those values are very close to the composition of the sample determined by TEM-EDS on large NP assemblies (43% at. and 62 % at. Pd, respectively).

For these two orientation relationships, the resulting morphologies exhibit the same surface indexes but the relative extension of the facets is not the same depending on a given orientation relationship. For example, in both morphologies, the total extension of the (111) and (100) facets is not the same. This structural difference can have an important influence on the catalytic activity of the NPs because it defines which crystallographic planes are in contact with the reacting gases. Finally, the dominant epitaxial relationship is not the same for the $Au_{57}Pd_{43}$ and $Au_{38}Pd_{62}$

compositions, suggesting the dependence of the Au-Pd/r-TiO_2 interface energy as a function of the alloy composition.

The catalytic performance of the supported NPs was evaluated in the gas-phase hydrogenation of butadiene. Three samples, $Au_{57}Pd_{43}$/r-TiO_2, $Au_{38}Pd_{62}$/r-TiO_2 and Pd/r-TiO_2, were compared. The reaction tests were carried out at room temperature and consisted of several runs. After each run, the gases in the reactor were evacuated during fifteen minutes before injecting a new gas mixture for the next cycle. Supported Au being poorly active for hydrocarbon hydrogenation at room temperature,[16] Au/r-TiO2 was not tested in the reaction.

Figure 6 reports the evolution of the partial pressures of butadiene, butene and butane as a function of time over $Au_{57}Pd_{43}$/r-TiO_2. The turnover frequency (TOF) is of 20 ± 2 butene molecules formed per surface metal atom per minute, which is of the order of what was previously measured under the same conditions on powder-supported Pd catalysts[42,43]. For TOF calculation, we have used the total number of metal atoms (Pd + Au) at the surface of the NPs, which were considered as spheres[44]. The spherical approximation is reasonable for FCC metals and truncated octahedra. The metal dispersion used was $1.1/d$ where d is the average metal particle size in nm. Surface segregation, if any, was not taken into account in this calculation. The surface composition was assumed equal to the average sample composition. Furthermore, butane is not formed during this run, i.e. the selectivity to butene is 100%.

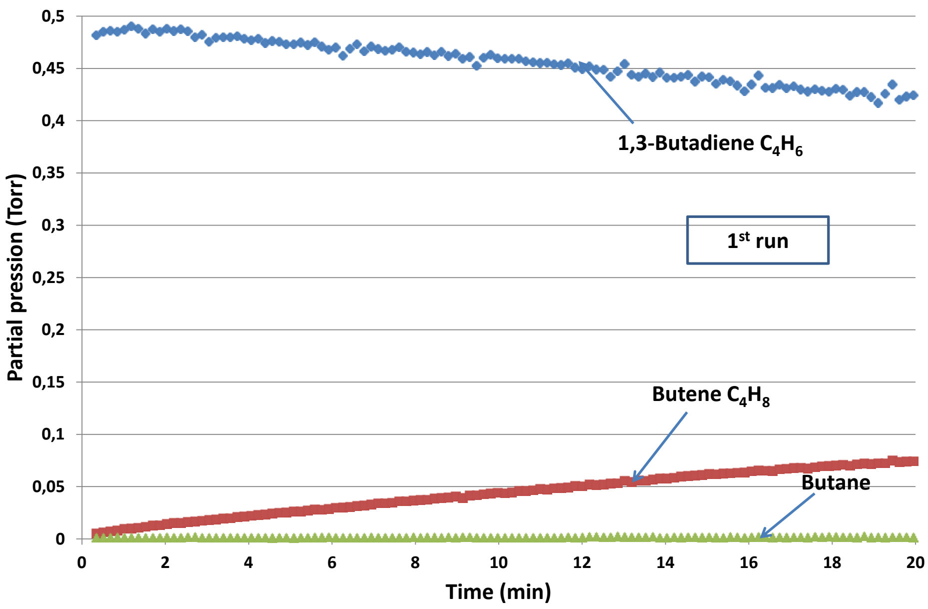

Figure 6 : Time evolution of the partial pressure of butadiene (blue rhombus), butene (red square) and butane (green triangle) over $Au_{57}Pd_{43}$/r-TiO_2 during the 1^{st} test run.

Figure 7 (a) to (c) shows the evolution of butene partial pressure during four consecutive catalytic runs over Pd/r-TiO_2, $Au_{38}Pd_{62}$/r-TiO_2 and $Au_{57}Pd_{43}$/r-TiO_2. Note that for all three catalysts, no butane was detected during the reaction, as already observed in Figure 6 for $Au_{57}Pd_{43}$/r-TiO_2. After the second run, the catalysts were treated under 10 Torr O_2 for 30 min then reduced under 10 Torr H_2 for 30 min. This type of oxidation-reduction treatment is widely used in heterogeneous catalysis to either activate the catalysts through decomposition of the precursors followed by reduction of the metal(s), or regenerate the catalysts by removing contaminants such as atomic carbon or coke accumulated on the catalyst surface during the reaction. The latter treatment allows one to increase the catalyst lifetime[45]. As shown in Figure 7c for the $Au_{57}Pd_{43}$/r-TiO_2 sample, the catalyst activity (butene formation rate) increases by a factor of ~4 after this treatment. This suggests that the carbon adsorbed at the metal surface during the sample transfer has been removed by the treatment.

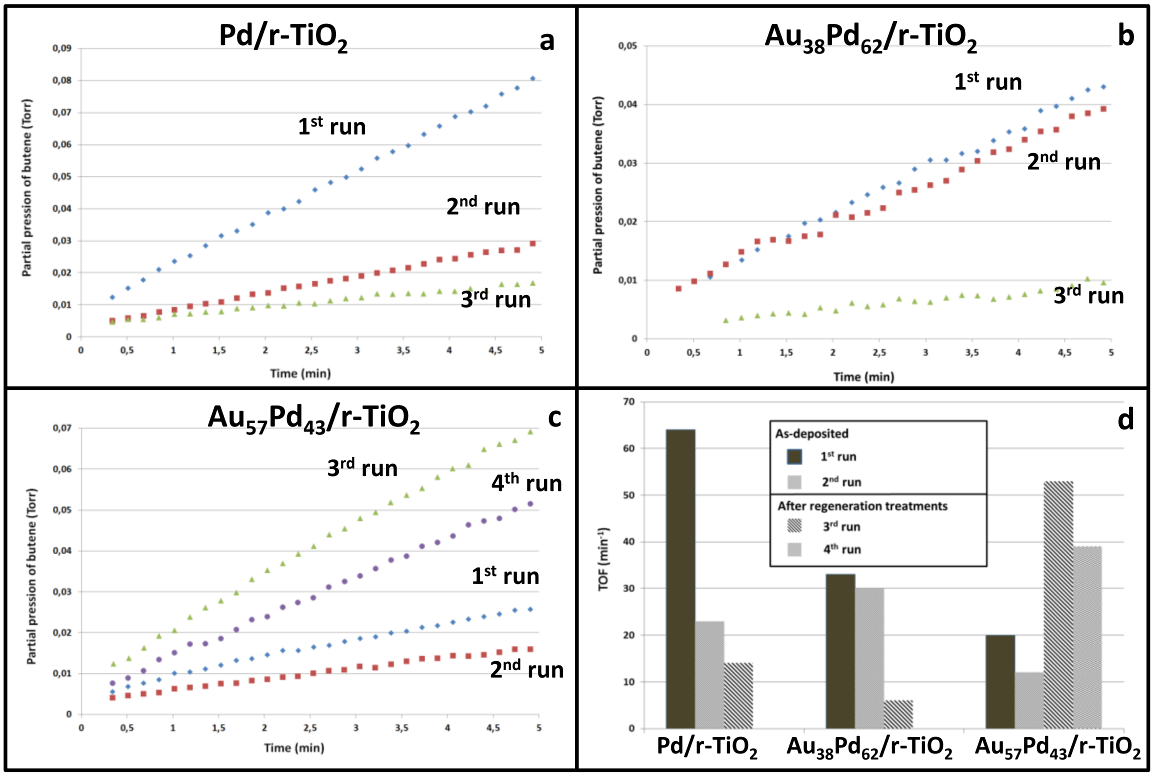

Figure 7 : (a-c) Time evolution of the partial pressure of butenes for Pd/r-TiO_2, $Au_{38}Pd_{62}$/r-TiO_2, and $Au_{57}Pd_{43}$/r-TiO_2; (d) Evolution of the turnover frequency (TOF) of butene formation along several test runs. Between the 2nd and 3rd runs, the catalyst was treated by oxidation under 10 Torr O_2 followed by reduction under 10 Torr H_2.

To better compare the activities of the three catalysts, Figure 7d depicts the evolutions of the TOFs of butene formation. Three main observations can be made: i) The initial activity (first run butene formation rate) decreases as the Au concentration increases; ii) Between the first and the second runs, all three catalysts exhibit a drop of activity, which is much more prominent in the case of Pd/r-TiO_2; iii) Upon the oxidation-reduction treatment, whilst $Au_{57}Pd_{43}$/r-TiO_2 strongly activates, the other two samples partially deactivate.

The decrease in initial activity as Au content increases (Fig. 7d) is due to the lesser availability of active Pd sites, Au being intrinsically poorly active in butadiene hydrogenation. The deactivation of the Pd catalyst from run 1 to run 2 is ascribed to the poisoning of active sites through gradual decomposition of hydrocarbons during the reaction. Gold appears to stabilize the NPs against poisoning, especially for the intermediate composition ($Au_{38}Pd_{62}$/r-TiO_2).

The most striking observation concerns the catalyst-dependent behavior after the calcination-reduction treatment. We tentatively relate this phenomenon to the effect of Au on Pd hydride formation. Palladium is the only noble metal which, in the bulk phase, absorbs hydrogen at room temperature and atmospheric H_2 pressure, and forms a stable concentrated hydride (β phase) for high H:Pd ratios[46]. The hydrogen absorption rate increases and the absorption capacity decreases upon nanosizing[47]. Moreover, the H absorption properties can be modulated by alloying palladium with another metal, with beneficial or detrimental effects on catalytic performance[48,49]. Hydrogen absorption may partially deactivate the Pd-rich Pd/r-TiO_2 and $Au_{38}Pd_{62}$/r-TiO_2 catalysts, as observed for single-crystals[27,50,51]. During the calcination-reduction treatment of Pd/r-TiO_2 and $Au_{38}Pd_{62}$/r-TiO_2 catalysts, it is likely that the deactivation induced by hydrogen absorption surpasses the beneficial effect of the catalyst surface regeneration, causing a net decrease in catalytic activity after treatment. In contrast, $Au_{57}Pd_{43}$/r-TiO_2 becomes four times more active after the treatment, which might be ascribed to the vanishing solubility of hydrogen in Au-Pd for Au-rich alloy compositions[52-54]. With hydrogen absorption being negligible in $Au_{57}Pd_{43}$/r-TiO_2, we expect the latter to fully benefit from the calcination-reduction treatment.

Moreover, we cannot exclude that the increase in catalytic activity of the $Au_{57}Pd_{43}$/r-TiO_2 sample after treatment is due to a change in the structure of the NPs during calcination-reduction. Indeed, it has been recently shown that, besides the chemically-disordered FCC structure, the phase diagram of Au-Pd nanoalloys displays long-range chemically-ordered phases[18]. Around near-equiatomic composition, Au-Pd nanoalloys show $L1_0$ long-range chemical order below 600 °C. In the present study, this ordered phase could appear in $Au_{57}Pd_{43}$ under hydrogen treatment and display enhanced activity in butadiene hydrogenation as compared to the as-synthesized FCC NPs.

CONCLUSION

In this work, model Au-Pd nanocatalysts supported on rutile titania nanorods were fabricated by pulsed laser deposition in vacuum at 300°C. The nanoalloys, with average diameter of 3.5 nm, present several shapes including droplet and truncated octahedron. The presence of non-equilibrium shapes is a strong indication of a weak degree of epitaxy between the Au-Pd particles and the r-TiO_2 support. The HRTEM images show that most of truncated octahedral particles are FCC single crystals oriented along the [101] zone axis and delimited by {111} and {100} facets. Statistical analysis of these particles evidences various epitaxial relationships with the rutile support. Two dominant epitaxial relationships were identified: Au-Pd (111) [101] // Rutile (110) [1-1-1] and Au-Pd (100) [101] // Rutile (110) [1-10], giving rise to two types of morphology.

These model catalysts appear active and selective for the partial hydrogenation of butadiene. The initial activity decreases as the Au content increases. However, while a calcination-reduction treatment partially deactivates the Pd-rich samples, it strongly activates the Au-rich Au-Pd catalyst. This is tentatively attributed to an improved catalyst resistance to hydriding for high Au concentrations.

A further step will consist in optimizing the synthesis conditions to obtain only equilibrium-shaped Au-Pd particles. This will allow us to link their catalytic properties with their 3D morphology, in particular the proportions of {111} and {100} facets. Further investigations by post-reaction

HRTEM or *in situ* TEM of Au-Pd/TiO_2 particles after butadiene hydrogenation tests will be undertaken to probe possible structural modifications due to the reaction and treatment conditions, such as hydriding and chemical ordering.

▪ AUTHOR INFORMATION

Corresponding Author

**Corresponding author: E-mail : jaysen.nelayah@univ-paris-diderot.fr*

Author Contributions

The manuscript was written through contributions of all authors. All authors have given approval to the final version of the manuscript and contributed equally.

Notes

The authors declare no competing financial interest

▪ ACKNOWLEDGMENTS

The authors acknowledge the support of the French Agence Nationale de la Recherche (ANR) under contract reference ANR-11-BS10-009. We are also grateful to the Region Ile-de-France for convention SESAME E1845 for the support of the JEOL ARM 200F electron microscope installed at the Paris Diderot University.

▪ REFERENCES

1. L. Piccolo, Surface studies of catalysis by metals : nanosize and alloying effects in Nanoalloys : Synthesis, Structure and Properties, 369-404, eds. D. Alloyeau, C. Mottet and C.

Ricolleau (Springer, London 2012).

2. M. Chen, D. Kumar, C. Yi, C.-W. and D.W. Goodman, The promotional effect of gold in catalysis by palladium-gold. (2005) *Science* **310**, 291–293.

3. J.K. Edwards *et al.* Direct synthesis of hydrogen peroxide from H_2 and O_2 using TiO_2-supported Au-Pd catalysts. (2005) *J. Catal.* **236**, 69–79.

4. D.I. Enach *et al.* Solvent-free oxidation of primary alcohols to andehydes using Au-Pd/TiO_2 catalysts. (2006) *Science* **311**, 362–365.

5. A. Hugon, L. Delannoy and C. Louis. Supported gold catalysts for selective hydrogenation of 1,3-butadiene in the presence of an excess of alkenes. (2008) *Gold Bull.* **2**, 127–138.

6. N. El Kolli, L. Delannoy and C. Louis. Bimetallic Au-Pd catalysts for selective hydrogenation of butadiene: Influence of the preparation method on catalytic properties. (2013) *J. Catal.* **297**, 79–92.

7. X. Yang *et al.* High performance Pd-Au bimetallic catalyst with mesoporous silica nanoparticles as support and its catalysis of cinnamaldehyde hydrogenation. (2012) *J. Catal.* **291**, 36–43.

8. P. Kittisakmontree *et al.* The liquid-phase hydrogenation of 1-heptyne over Pd-Au/TiO_2 catalysts prepared by the combination of incipient wetness impregnation and deposition-precipitation. (2013) *J. Catal.* **297**, 155–164.

9. Q. Xu *et al.* TEM study on catalysis deactivation during selective acetylene hydrogenation. (2005) *Microsc. Microanal.* **11**, 1576–1577.

10. G.J. Hutching, Catalysis by gold. (2005) *Catal. Today* **100** (1-2), 55–61.

11. F. Cardénas-Lizana and M.A. Keane. The development of gold catalysts for use in hydrogenation reactions. (2013) *J. Mater. Sci.* **48**, 543–564.

12. L. McEwan, M. Julius, S. Roberts and J.C.Q. Fletcher. A review of the use of gold catalysts in selective hydrogenation reactions. (2010) *Gold Bull.* **43**, 298–306.

13. Bus, E. & van Bokhoven, J. A. Hydrogen chemisorption on supported platinum, gold and platinum-gold alloy catalysts. *Phys. Chem. Chem. Phys.***9**, 2894–2902 (2007).

14. G.H. Hutchings and C.J. Kiely, Strategies for the Synthesis of Supported Gold Palladium Nanoparticles with Controlled Morphology and Composition. (2013) *Acc. Chem. Res.*, ***46*** **(8)**, 1759–1772

15. A. Villa, D. Wang, D.S. Su and L. Prati, New challenges in gold catalysis: bimetallic system, (2015) *Catal. Sci. Technol.* **5**, 55-68.

16. Z. Konuspayeva *et al.*, Au–Rh and Au–Pd nanocatalysts supported on rutile titania nanorods: structure and chemical stability, (2015) *Phys. Chem. Chem. Phys.*, **17**, 28112-28120.

17. A. Hugon, L. Delannoy, J.-M. Krafft and C. Louis, Selective hydrogenation of 1,3-butadiene in the presence of an excess of alkenes over supported bimetallic gold-palladium catalysts. (2010) *J. Phys. Chem. C* **114,** 10823–10835.

18. J. Nelayah, N.T. Nguyen, D. Alloyeau, G.Y. Wang and C. Ricolleau, Long-range chemical orders in Au-Pd nanoparticles revealed by aberration-corrected electron microscopy, (2014) *Nanoscale* **6** (17) 10423-10430.

19. N.T NGuyen, PhD Thesis: Synthesis and study of structural, thermodynamical and catalytic properties of bimetallic Au-Pd nanocatalysts by using aberration corrected electron microscopy, (2015) University Paris Diderot, France.

20. H. Li and P. Afanasiev, On the selective growth of titania polymorphs in acidic aqueous medium. (2011) *Mater. Res. Bull.* **46,** 2506–2514.

21. H. Li *et al.* Hydrothermal synthesis and acidity characterization of TiO_2 polymorphs. (2013 *Mater.Res. Bull.***48,** 3374–3382).

22. Y. Kohno *et al.* Development of a cold field-emission gun for a 200kV atomic resolution electron microscope. (2010) *Microscopy and Analysis (Supplement)* **24,** S9–S13.

23. M. Haider *et al.* Electron microscope image enhanced. (1998) *Nature* **392,** 768–769.

24. C. Ricolleau *et al.* Performances of an 80-200 kV microscope employing a cold-FEG and an aberration-corrected objective lens. (2012) *J. Electron Microsc.* **62,** 283–293.

25. G. Cliff and G.W. Lorimer, The quantitative analysis of thin specimens. (1975) *J. Microsc.***103,** 203–207.

26. F. Morfin and L. Piccolo. A versatile elevated-pressure reactor combined with an ultrahigh vacuum surface setup for efficient testing of model and powder catalysts under clean gas-phase conditions. (2013) *Rev. Sci.c Instr.***84,** 1–7.

27. A. Valcarcel, F. Morfin and L. Piccolo. Alkene hydrogenation on metal surfaces: Why and when are Pd overlayers more efficient catalysts than bulk Pd? (2009) *J. Catal.* **263**, 315-320.

28. E. Ringe, R.P. Van Duyne and L.D. Marks. Wulff construction for alloy nanoparticles.

(2011) *Nano Letters* **11,** 3399–3403.

29. F. Cosandey, L. Zhang and T.E. Madey. Effect of substrate temperature on the epitaxial growth on TiO_2 (110). (2001) *Surf.Sci.***474,** 1–13.

30. T. Okazawa *et al.* Growth mode and electronic structure of Au nano-clusters on NiO (001) and TiO_2 (110). (2006) *Surf. Sci.* **600,** 1331–1338.

31. F. Cosandey and T.E. Madey. Growth, morphology, interfacial effects and catalytic properties of Au on TiO_2. (2001) *Surf. Rev. Lett.* **8,** 73–93.

32. L. Zhang, F. Cosandey, R. Persaud and T.E. Madey. Initial growth and morphology of thin Au films on TiO_2 (110). (1999) *Surf. Sci.* **439,** 73–85.

33. T. Akita, K. Tanaka, S. Tsubota and M. Haruta. Analytical high-resolution TEM study of supported gold catalysts: orientation relationship between Au particles and TiO_2 supports. (2000) *J. Electron Microsc.* **49,** 657–662.

34. S. Ichikawa *et al.* Electron holographic 3-D nano-analysis of Au-TiO_2 catalyst at interface. (2003) *J. Electron Microsc.* **52,** 21–26.

35. T. Suzuki and R. Souda. The encapsulation of Pd by the supporting TiO_2 (110) surface induced by strong metal-support interactions. (2000) *Surf. Sci.e* **448,** 33–39.

36. M. Ahmadi et al., Shape-selection of thermodynamically stabilized colloidal Pd and Pt nanoparticles controlled via support effects, (2015) *J. Phys. Chem. C* **119**, 29178-29185

37. M. Ahmadi, F. Behafarid and B. R. Cuenya, Size-dependent adhesion energy of shape-selected Pd and Pt nanoparticles, (2016) *Nanoscale* **8**, 11635-11641.

38. C. M. Yim, C. L. Pand, D. R. Hermoso, C. M. Dover, C. A. Muryn, F. Maccherozzi, **S. S.**

Dhesi, R. Pérez and G. Thornton, Influence of support morphology on the bonding of molecules to nanoparticles. (2015) *PNAS* **112 (26)**, 7903-7908

39. S. Stemmer, P. Pirouz, Y. Ikuhara and R.F. Davis. Film/Substrate orientation relationship in the AlN/6H-SiC epitaxial system. (1996) *Phys. Rev. Lett.*, **77**, 1797-1800.

40. T. Akita, K. Tanaka, S. Tsubota and M. Haruta, Analytical high-resolution TEM study of supported gold catalysts: orientation relationship between Au particles and TiO_2 supports. (2000) *J. Electron Microsc.* **49**, 657 – 662.

41. L. Vegard, Die konstitution der mischkristalle und die raumfüllung der atome. (1921) *Z. Phys.* **5**, 17–26.

42. L. Piccolo, A. Valcarcel, M. Bausach, C. Thomazeau, D. Uzio and G. Berhault. Tuning the shape of nanoparticles to control their catalytic properties: selective hydrogenation of 1,3-butadiene on Pd/Al_2O_3 (2008) *Phys. Chem. Chem. Phys*. **10**, 5504-5506.

43. J. Martins *et al*. Improving the catalytic performances of metal nanoparticles by combining shape control and encapsulation. (2015) *Appl. Catal. A* **504**, 504-508.

44. T.S. Nguyen, F. Morfin, M. Aouine, F. Bosselet, J.L. Rousset and L. Piccolo, Trends in the CO oxidation and PROX performances of the platinum-group metals supported on ceria (2015) *Catal. Today* **253**, 106–114

45. E. Furimsky and F.E. Massoth. Introduction of regeneration of hydroprocessing catalysts. (1993) *Catal.Today* **17,** 537–659.

46. D.N. Jewett and A.C. Makrides. Diffusion of hydrogen through palladium and palladium-silver alloys. (1964) *Trans. Faraday Soc.* **61,** 932–939

47. C. Langhammer, V.P. Zhdanov, I. Zorić and B. Kasemo. Size-dependent kinetics of hydriding and dehydriding of Pd nanoparticles. (2010) *Phys. Rev.Lett.* **104**, 135502.

48. H. Kobayashi, M. Yamauchi, R. Ikeda and H. Kitagawa. Atomic-level Pd-Au alloying and controllable hydrogen-absorption properties in size-controlled nanoparticles synthesized by hydrogen reduction. (2009) *Chem. Commun.* 4806–4808.

49. C. Zlotea *et al.* Nanoalloying bulk-immiscible iridium and palladium inhibits hydbride formation and promotes catalytic performances. (2014) *Nanoscale* **6,** 9955–9959.

50. L. Piccolo, A. Piednoir and J.C. Bertolini. Pd-Au single-crystal surfaces : Segregation properties and catalytic activity in the selective hydrogenation of 1,3-butadiene. (2005) *Surf. Sci.* **592,** 169–181.

51. L. Piccolo, A. Piednoir and J.C. Bertolini. Absorption and oxidation of hydrogen at Pd and Pd–Au (1 1 1) surfaces. (2006) *Surf. Sci.* **600** (18), 4211-4215.

52. B.J. Joice, J. J. Rooney, P.B. Wells and G.R. Wilson. Nature and reactivity of intermediates in hydrogenation of buta-1,3-diene catalyzed by cobalt and palladium-gold alloys. (1966) *Disc. Faraday Soc.* **41,** 223–236.

53. A. Maeland and T.B. Flanagan. X-Ray and thermodynamic studies of the absorption of hydrogen by Gold-Palladium alloys. (1965) *J. Phys. Chem.* **69** (10), 3575 - 3581.

54. S. Luo, D. Wang, T.B. Flanagan. Thermodynamics of Hydrogen in fcc Pd−Au Alloys. (2010) *J. Phys. Chem. B* **114 (18)**, 6117-6125.

For Table of Contents Use Only

Manuscript title: Structural properties of catalytically-active bimetallic gold-palladium nanoparticles synthesized on rutile titania nanorods by pulsed laser deposition

Author list : N. Tai Nguyen, Jaysen Nelayah, Pavel Afanasiev, Laurent Piccolo, Damien Alloyeau, and Christian Ricolleau

TOC graphic

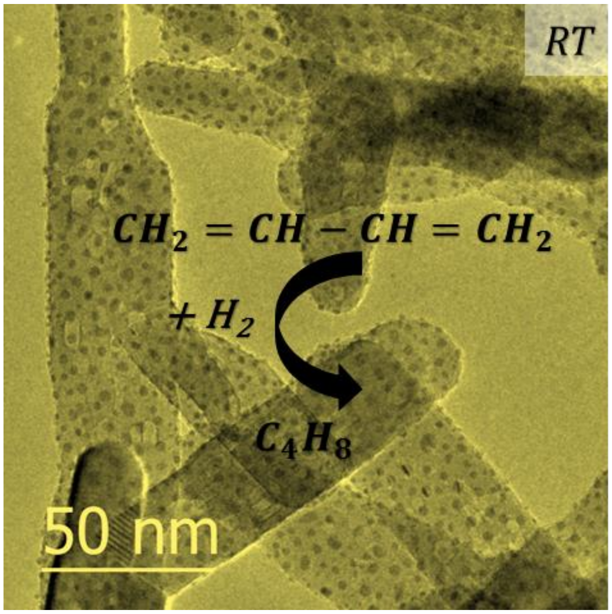

Synopsis : The atomic structure of TiO_2-supported gold-palladium nanoparticles fabricated by pulsed laser deposition were studied at the atomic scale using aberration-corrected transmission electron microscopy. Both single crystalline and polycrystalline nanoparticles were observed. Different epitaxial relationships between the Au-Pd nanoparticles and their supports were identified. The bimetallic Au-Pd nanoparticles are both active and selective in the partial hydrogenation of 1,3-butadiene.